Homogenization Methods for Thermal Study of Support Structure in Laser Powder Bed Fusion (L-PBF) -Application to Process Numerical Modeling

Yancheng Zhang, Hugo Behlal, Charles-André Gandin, Oriane Senninger, Gildas Guillemot, Michel Bellet

Homogenization Methods for Thermal Study of Support Structure in Laser Powder Bed Fusion (L-PBF) - Application to Process Numerical Modeling

Abstract

This manuscript reports on a homogenized model for the anisotropic thermal conductivity of support structures constructed by the laser powder bed fusion (L-PBF) process, and its application to the numerical simulation of the L-PBF process. Considering both analytical and numerical approaches, the model is developed across a temperature interval encompassing the entire L-PBF process. Subsequently, the homogenized material properties are incorporated into a thermal finite element model (FEM) of the L-PBF process to consider the effects of the support structures, taking into account their anisotropic properties. The simulation results of the L-PBF process indicate that the support structures act as a thermal barrier, retaining more heat in part compared to direct printing on the substrate. The implementation of homogeneous thermal conductivity in the L-PBF process simulation demonstrates its efficiency and potential application to better control heat transfer during part construction.

Keywords: Additive manufacuring L-PBF, Support structure, Thermal analysis, Homogenization, Numerical simulation

1. Introduction

Owing to the flexible scanning laser path, the laser powder bed fusion (L-PBF) based additive manufacturing (AM) process offers the possibility of creating complex, high-added value metal parts with good dimensional accuracy (Martin et al., 2017). However, these complex parts may include overhanging features which pose significant challenges during the manufacturing process, as they may lead to the creation of fragility or even the collapse of the part if not properly supported (Yang et al., 2023). Adding support structures, as illustrated in Fig. 1, prevents warping, collapse, and cracks that result from thermal stresses (Kajima et al., 2018). Additionally, they facilitate the removal of the part from the substrate in the later stages of the process. However, the thickness of the support is usually less than 1 mm (Zhang & Li, 2022), and the layers consisting of powder bed support show less than 10 % thermal conductivity compared to fully condensed counterparts (Subedi et al., 2022), acting as a thermal insulator. Thus, adding support structures to the part during the printing process has a strong impact on the thermal diffusion and the temperature distribution within the part (Yue et al., 2023). As the thermal condition constitutes the initial phase for subsequent metallurgical and mechanical responses, investigating the thermal distribution and its evolution in the printed part while considering the support is highly demanded.

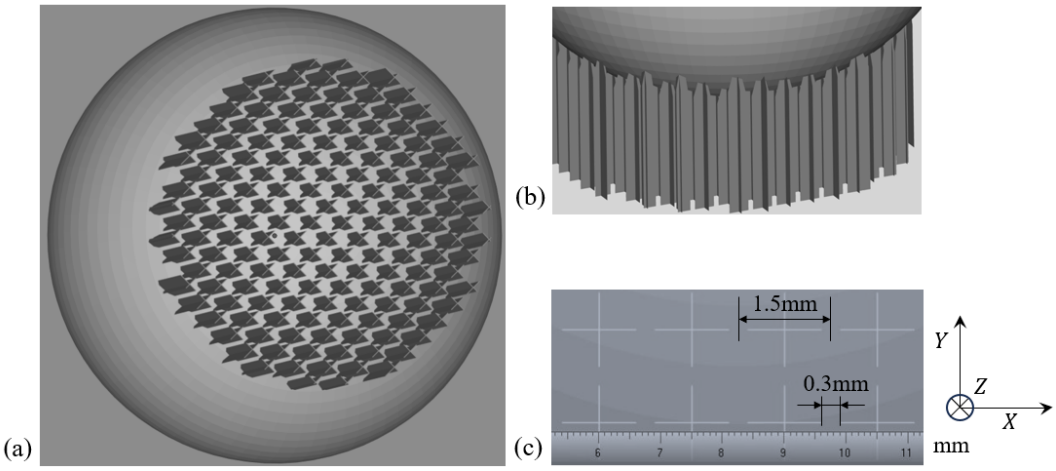

Figure 1. Computer aided design representations showing the unit cross pattern support for an additively manufactured ball geometry by laser powder bed fusion with (a) a global bottom view of the printed surface including the network of crosses serving as support of the ball on the substrate, (b) an enlarged front view focused on the support and (c) the size of the unit cross pattern in a cross section perpendicular to the building direction.

Observing the temperature evolution or distribution within components manufactured by L-PBF experimentally poses significant challenges. The local evolution encountered during the L-PBF process makes challenging to capture precise temperature variations using traditional sensors, mainly due to limitations in spatial and temporal resolution. Furthermore, restricted access to the build area, primarily caused by the presence of non-melted powder, along with extreme conditions such as high temperatures, further complicates the use of same sensors (Mahadevan et al., 2022). Consequently, researchers often turn to numerical simulations, such as the ones based on finite element modeling, to predict and analyze the temperature distribution within these components (Chen, 2019). Khobzi et al. (2022) proceeded to a finite element thermal simulation of the printing of a cantilever plate with block-type supports, each of several millimeter size, considering their exact geometries. These simulations, although reliant on experimental validations, offer a valuable tool for understanding and investigating the temperature field evolution, providing insights that may be difficult to obtain solely through experimental means.
However, the thin-walled structures usually adopted for the support (Jarvinen et al., 2014) are difficult to incorporate in the simulation as their fine geometrical details make the mesh generation very challenging and significantly increase computational expense. A common way to address this issue is to work with a homogeneous model for the support structure (March et al., 2023). Homogenization is a mathematical method employed to forecast the overall material characteristics at the macro (global) scale by analyzing the behavior of materials at either the micro or meso (local) scale. A medium can be homogenized analytically or numerically (Wang & Pan, 2008) and for various properties including mechanical (Terada et al., 2000; Liu & Shapiro, 2016) and thermal (Willot et al., 2013; Al Amin et al., 2018; Jin et al., 2017; Wu et al., 2013; El Moumen et al., 2015) ones. Such approaches are regularly used in the literature for composite materials (Burger et al., 2016) and porous media (Nakayama, 2023). However, only a few papers discuss the effective properties of support structures in the L-PBF process.

Among them, ~~Liang et al.~~ Liang et al. (2020) performed an asymptotic homogenization of the anisotropic elastic properties of a thin-walled lattice support structure. They validated their approach experimentally through residual deformation measurement, enabling the implementation of the support as a solid continuum in a part-scale finite element simulation. This homogenized model significantly reduced the computing time by a factor of 10.

However their work was exclusively focused on the effective mechanical properties of the support, and few prior works were performed on effective thermal conductivity for support structures in L-PBF. ~~Zeng et al.~~ Zeng et al. (2015) realized both analytical and numerical homogenization on a representative volume element (RVE) to determine the effective vertical thermal conductivity of the support structures. Yet, the anisotropy of the thermal conductivity of the support and its application for process simulation was not investigated, especially for the low thermal conductivity metals such as nickel-based superalloys. This will ultimately impact phase transformations in solidification stage (He & Webler, 2022) as well as in the solid state (Krakhmalev & Kazantseva, 2021).

In this paper, the homogenized thermal conductivity of a typical cross-structured support system and its impact on the fabricated component are studied. In Section 2, the selection for an RVE is presented. Following this, the homogenized anisotropic thermal properties by combining numerical and analytical methods are characterized in Section 3. The anisotropic thermal conductivity is implemented in a non-linear thermal solver, followed by the numerical validation of the homogenized properties. Subsequently, in Section 4, the application to L-PBF process simulation is executed to evaluate the thermal influence of the supports. Finally, some conclusions are drawn in section 5.

Nomenclature

To enhance the readability of this paper, the notation of the vectors, matrices, variables related to support structure, process simulation and corresponding abbreviations are summarized in Table I.

2. Selection of a representative volume element (RVE)

As given in Fig. 2(a), a simple configuration is studied made of a grid pattern of thin cross-shaped structures, oriented vertically along the build direction z. The architecture is the same as in Fig. 1, but the dimensions are different. The wall thickness is 0.05 mm and the wall length is 0.8 mm, with a gap of 0.1 mm for each cross, as schematized in Fig. 2(b). Yellow regions denote the thin walls made of dense fused metal embedded within non-scanned powder, represented by the orange regions.

Considering the periodicity of the support geometry, there are multiple choices to define a representative volume element (RVE): for instance the one aligned with the wall reference frame (X, Y, Z), limited by the red contour, or the one aligned on a reference frame rotated with respect to the previous one by 45°, limited by the black contour. Note that the first one appears more favorable to conduct an analytical evaluation of the homogenized properties of the support structure, as this will be shown further.

TABLE I. Nomenclature

Variables for the support structure			
w	Support wall	p	Powder bed
(X, Y, Z)	RVE reference frame	(x, y, z)	Global reference frame
∇T_I	Thermal gradient along direction $I \in X, Y, Z$	$T_i, i \in 1, .., 6$	Isothermal temperature within RVE
$\langle x \rangle$	Homogenized value	$\{\}$	Mixture by the Heaviside function of level-set
$\boldsymbol{q}$	Heat flow vector	q_I	I component of $\langle \boldsymbol{q} \rangle$, $I \in X, Y, Z$
$\boldsymbol{q}_w$	Heat flow through dense wall	$q_{w,I}$	I component of $\boldsymbol{q}_w$, $I \in X, Y, Z$
$\boldsymbol{q}_p$	Heat flow through non-scanned powder	$q_{p,I}$	I component of $\boldsymbol{q}_p$, $I \in X, Y, Z$
q_1, q_2	Heat flow through non-scanned powder and wall	S_{total}	Total surface of RVE cross-section along Z
S_p	Powder surface of RVE cross-section along Z	S_w	Wall surface of RVE cross-section along Z
a, b	Characterized lengths within the RVE	α	ratio b/a
$\boldsymbol{e}_Z$	Unit vector along z axis	θ	RVE orientation angle
ϕ	Porosity	∇T^{imp}	Imposed temperature gradient
Variables related to thermal conductivity			
κ_w	Thermal conductivity of the support wall	κ_p	Thermal conductivity of non-scanned powder
$\mathbf{K}\|_{XYZ}$	Homogenized tensor in RVE reference frame	$\langle \kappa \rangle_{IJ}$	IJ component of $\mathbf{K}\|_{XYZ}$, $I, J \in X, Y, Z$
$\mathbf{K}\|_{xyz}$	Homogenized tensor in global reference frame	$\langle \kappa \rangle_{ij}$	ij component of $\mathbf{K}\|_{xyz}$, $i, j \in x, y, z$
$\mathbf{I}$	Unit tensor		
Process parameters and numerical modeling			
P_L	Laser power	v_L	Scanning speed
Δz	Layer thickness	$L \times W \times H$	Length, width and height
ϕ_L	Laser spot diameter	n_L	Scaling coefficient
t_{heat}	Numerical heating time	t_{scan}	Laser scanning time
t_{cool}	Numerical cooling time	t_D	Dwell time
$\dot{Q}_V$	Volume heat source	R	Reflection coefficient
Ω	Simulation domain	H_D	Hatch distance
m	Mass	ρ	Density
h	Enthalpy	C_p	Specific heat
$C_{p,p}$	C_p for powder	$C_{p,w}$	C_p for support wall
$h_{conv.}$	Heat exchange coefficient	T_{ext}	Environment temperature
$\boldsymbol{n}$	Unit normal vector	n	Deposition layer
ψ	Level set function	V_{layer}	Volume of energy deposition
Abbreviation			
AM	Additive manufacturing	L-PBF	Laser powder bed fusion
RVE	Representative volume element	FEM	Finite element model

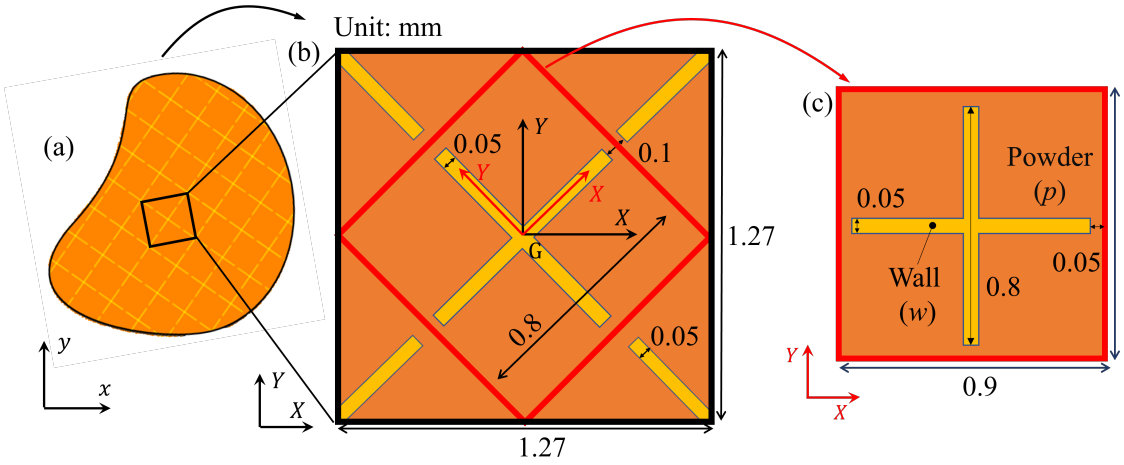

Figure 2. (a) A transverse cross section, perpendicular to the build direction, of the support structure studied in this work. Extraction of two different RVEs: limited by black contour (b) and red contour (c).

3. Characterization of the anisotropic conductivity tensor

The objective of this Section is first to determine the homogenized tensor for thermal conductivity $\mathbf{K}|_{XYZ}$ in the walls-aligned reference frame (X, Y, Z) limited by the red contour, and second to deduce the homogenized tensor $\mathbf{K}|_{xyz}$in the global reference

frame (x, y, z). Given the simplicity of the RVE's geometry, both analytical and numerical solutions will be considered to proceed to the homogenization process. These approaches are detailed in Sections 3.1 and 3.2 hereunder. Furthermore, a numerical verification is conducted to confirm the homogenization process in Section 3.3.

3.1. Analytical solution

The efforts will focus on the characterization of the thermal conductivity in both vertical (Z) and horizontal ($\perp Z$) axes of the RVE, corresponding to the diagonal terms of the $\mathbf{K}|_{XYZ}$ tensor. Then, it will be numerically demonstrated that it is reasonable to assume that non-diagonal terms can be neglected.

3.1.1. Analytically homogenized vertical conductivity

The RVE geometry being invariant along the Z axis, in view of characterizing the homogenized vertical conductivity, we model a vertical heat flow going through the RVE by a fixed overall vertical thermal gradient ∇T_Z. This heat flow diffuses in parallel through two materials: the dense walls (index w), and the non-scanned powder (index p). As a result, the heat flow along Z axis through each of the two materials and through the homogenized material, respectively $q_{w,Z}$, $q_{p,Z}$ and $\langle q \rangle_Z$ can be expressed by:

$$q_{w,Z} = -\kappa_w \nabla T_Z \tag{1a}$$

$$q_{p,Z} = -\kappa_p \nabla T_Z \tag{1b}$$

$$\langle q \rangle_Z = -\langle \kappa \rangle_{ZZ} \nabla T_Z \tag{1c}$$

where κ_w is the thermal conductivity of the support wall, κ_p is the non-scanned powder's thermal conductivity, $\langle \kappa \rangle_{ZZ}$ is the homogenized thermal conductivity along Z direction, where the angle bracket $\langle \cdot \rangle$ defines the homogenized property in the mixed structure and powder domain. Note here that the heat conductivity of the dense metal is assumed isotropic. The apparent conductivity of the powder, much lower than κ_p, is also assumed isotropic, and derives itself from an homogenization process. Models for apparent conductivity of powder beds can be found in the literature, see for instance ~~Hadley~~ Hadley (1986).

For the RVE cross-section visible in Fig.2 (c), let S_{total}, S_p and S_w be respectively the total surface, the powder surface and the wall surface, with $S_{total} = S_p + S_w$. Because the lateral surfaces (parallel to the Z axis) act as symmetry planes, the homogenized heat flow $\langle \boldsymbol{q} \rangle$ is necessarily oriented along Z. It is assumed (this hypothesis will be discussed later in light of the numerical simulation) that $\boldsymbol{q}_w$ and $\boldsymbol{q}_p$ are essentially oriented along Z, despite the strong difference between the conductivities κ_w and κ_p. Hence we can write:

$$\langle q \rangle_Z S_{total} = q_{w,Z} S_w + q_{p,Z} S_p \tag{2}$$

Injecting Eq.1 into Eq.2 gives :

$$\langle \kappa \rangle_{ZZ} = \kappa_w \frac{S_w}{S_{total}} + \kappa_p \frac{S_p}{S_{total}} \tag{3}$$

The homogenized vertical conductivity depends only on the conductivity ratio and surface ratio between support walls and powder. It can also be noted that $S_w / S_{total} \ll 1$

(while $S_p/S_{total} <\sim 1$). Consequently, $\langle\kappa\rangle_{ZZ}$ can be found more or less close to κ_p, depending on the conductivity and the surface ratio.

3.1.2. Analytically homogenized horizontal conductivity

Parallel isothermal surfaces (PIS)

According to ~~Gori and Corasaniti~~ Gori & Corasaniti (2014), the assumption of parallel isothermal surfaces (PIS) consists in considering that thermal conductivity in the direction perpendicular to the flow is infinitely high, this direction being perpendicular to X in the present investigated case. Considering a RVE with solid walls aligned along X and Y, this gives rise to isothermal zones delimited only by the X coordinate when imposing a flux along X. Fig. 3a illustrates the three isothermal zones with assigned colors: yellow - only powder, orange - mainly powder and red - mainly support wall. The effective thermal conductivity in the X direction, indicated by $\langle\kappa\rangle_{XX}$, is calculated by defining that the temperature at $X = 0$ is T_1, at $X = b$ is T_2, at $X = a + b$ is T_3, at $X = a + 2b$ is T_4, at $X = 2a + 2b$ is T_5, and at $X = 2a + 3b$ is T_6.

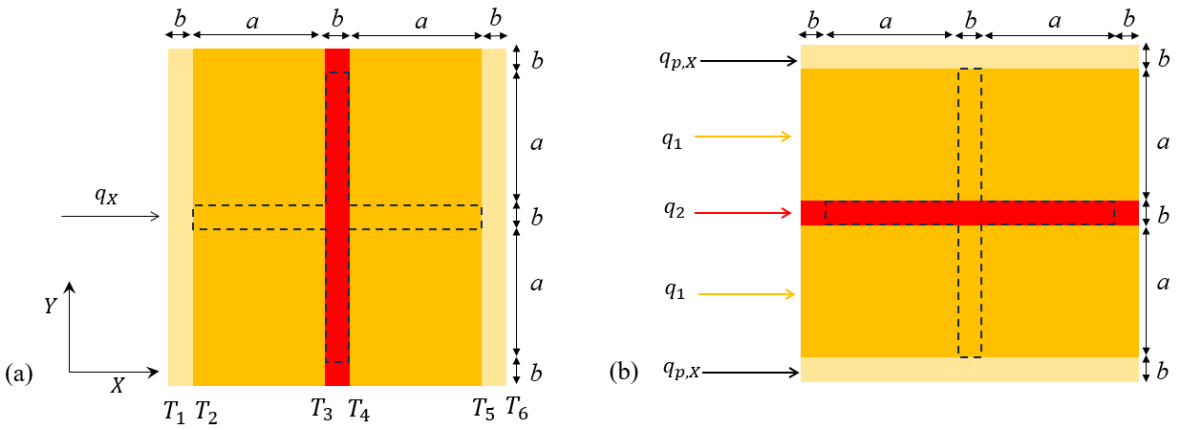

Figure 3. Representation of zones defined by the hypotheses: (a) the parallel isothermal surfaces (PIS) and (b) the parallel flow surfaces (PFS)

With a similar idea of reference Gori & Corasaniti (2014) to deal with support wall and powder bed, assuming that $q_X = \langle q\rangle_X$ is equal for each isothermal zone along X direction (yellow, orange, red) and defining a ratio $\alpha = b/a$, the effective steady-state conductivity of the RVE under the PIS assumption can be determined by:

$$\frac{1}{\langle\kappa\rangle_{XX}^{PIS}} = \frac{2\alpha}{\kappa_p(2+3\alpha)} + \frac{2}{2\kappa_p(1+\alpha)+\kappa_w\alpha} + \frac{\alpha}{2\kappa_p\alpha+\kappa_w(2+\alpha)} \tag{4}$$

Parallel heat flux surfaces (PFS)

The assumption of parallel flow surfaces (PFS) means that the components of the thermal conductivity in the directions perpendicular to the heat flow are assumed to be zero. This gives rise to parallel flow surfaces. Fig. 3 b illustrates each colored area as a iso-heat flow, in which the value of the flux is invariant along the X axis. As a result, $\langle q\rangle_X = 2q_{p,X} + 2q_1 + q_2$

For the studied RVE geometry, the effective steady-state conductivity of the RVE under the PFS assumption can be obtained:

$$\langle\kappa\rangle_{XX}^{PFS} = \kappa_p \left(\frac{2\alpha}{2+3\alpha} + \frac{2\kappa_w}{2\kappa_w\left(1+\alpha\right)+\kappa_p\alpha} + \frac{\kappa_w\alpha}{2\kappa_w\alpha+\left(2+\alpha\right)\kappa_p} \right) \tag{5}$$

3.1.3. Temperature dependence of analytical homogenized conductivities

Based on the different analytical solutions presented in the Sections above, the effective thermal conductivity as a function of temperature is given in Fig. 4 for Inconel 738 with a low carbon version (IN738LC), where the thermal conductivity of support wall (the condensed part) is from the work of ~~Grange et al.~~ Grange et al. (2021), and the powder conductivity is based on the model of ~~Hadley~~ Hadley (1986) with a porosity of 0.5. The effective thermal conductivity along vertical direction $\langle\kappa\rangle_{ZZ}$ (red dashed line, in Fig. 4a) lies between thermal conductivity curves of support wall and powder. As the ratio of the support wall is close to 9.6 %, the curve of $\langle\kappa\rangle_{ZZ}$ approaches powder matrix property. As critical assumptions are made for PIS and PFS, $\langle\kappa\rangle_{XX}^{PIS}$ and $\langle\kappa\rangle_{XX}^{PFS}$ represent the two bounds for $\langle\kappa\rangle_{XX}$ in Fig. 4b. Finally, the harmonic mean is proposed on the basis of Eq. 6.

$$\frac{1}{\langle\kappa\rangle_{XX}} = \frac{1}{2}\left(\frac{1}{\langle\kappa\rangle_{XX}^{PIS}} + \frac{1}{\langle\kappa\rangle_{XX}^{PFS}} \right) \tag{6}$$

The numerical characterization will be reported in next Section 3.2.

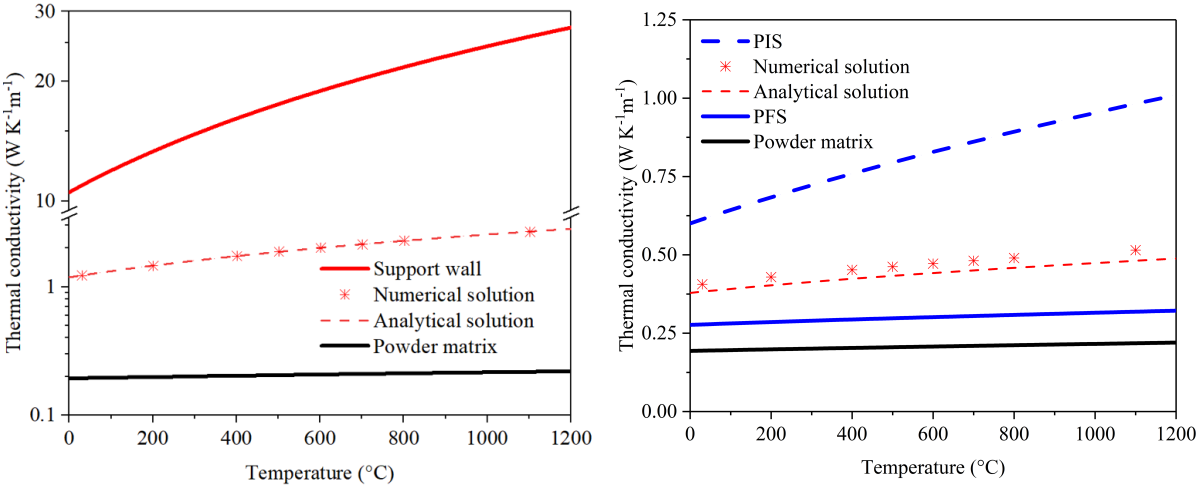

(a) Vertical direction, $\langle\kappa\rangle_{ZZ}$

(b) Horizontal direction, $\langle\kappa\rangle_{XX}$

Figure 4. Comparison of homogenized thermal conductivities (vertical and horizontal) as determined analytically (continuous and dashed curves) and numerically (red crosses)

3.2. Numerical solution

To verify the validity of the analytical expressions obtained in the previous Section, numerical characterizations are carried out to estimate the RVE's homogenized thermal conductivity in the different directions. The numerical model of the same RVE as for the previous analytical approach (aligned on dense solid walls) is shown in Fig. 5. Note that its height H can be chosen arbitrarily (here $H = 2$ mm). The RVE is meshed with tetrahedral linear finite elements, with refinement around the interface between

the dense metal and the non-melted powder. To identify this interface within the mesh, the level set framework is adopted. Accordingly, properties of the dense metal and the non-melted powder are mixed within a transition zone around the interface, by use of a mixture law based on a smooth Heaviside function evolving from 0 to 1. The mesh size is in between 5 μm in the interfacial region and 50 μm in the powder zone. The transition half-thickness, $\epsilon = 25$ μm, is considered near the interface. As a result, there are about 10 elements in the transition zone, indicating a stabilized transition for the two materials.

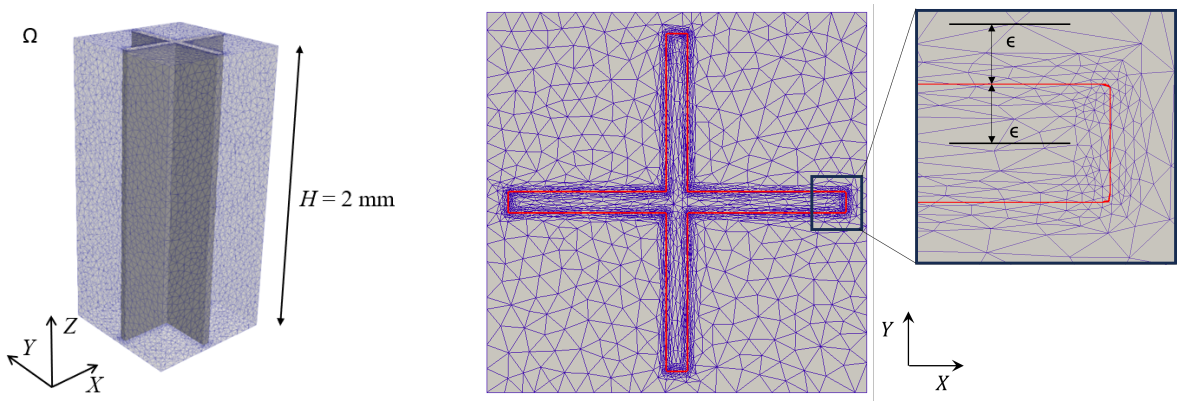

(a) 3D view of the mesh geometry (b) Top view of the mesh

Figure 5. Discretized finite element mesh for numerical characterization

The numerical identification of the components of tensor $\langle \mathbf{K} \rangle$ consists in imposing a series of prescribed thermal gradient ∇T, by defining appropriate boundary conditions along the border of the RVE. Then, for each prescribed gradient the heat transfer problem is solved in the RVE, to obtain a steady-state temperature distribution. From that, the homogenized heat flux vector $\langle \boldsymbol{q} \rangle$ can be calculated, and finally, tensor components can be identified by use of the relation:

$$\langle \boldsymbol{q} \rangle = \begin{bmatrix} \langle q \rangle_X \\ \langle q \rangle_Y \\ \langle q \rangle_Z \end{bmatrix} = - \langle \mathbf{K} \rangle \nabla T = - \begin{bmatrix} \langle \kappa \rangle_{XX} & \langle \kappa \rangle_{XY} & \langle \kappa \rangle_{XZ} \\ \langle \kappa \rangle_{YX} & \langle \kappa \rangle_{YY} & \langle \kappa \rangle_{YZ} \\ \langle \kappa \rangle_{ZX} & \langle \kappa \rangle_{ZY} & \langle \kappa \rangle_{ZZ} \end{bmatrix} \begin{bmatrix} \nabla T_X \\ \nabla T_Y \\ \nabla T_Z \end{bmatrix} \tag{7}$$

The identification process is explained in more details in the following Section.

3.2.1. Numerically homogenized vertical conductivity

For the characterization of the vertical homogenized thermal conductivity, a vertical upward temperature gradient is applied to the RVE structure. The characterization steps are as follows:

- Dirichlet boundary conditions are applied to the top and bottom faces of the numerical model (respectively T_{top} and T_{bot} temperatures), while maintaining adiabatic conditions along the lateral surfaces. This defines an overall imposed temperature gradient, $\nabla T^{imp} = (T_{top} - T_{bot}) / H \boldsymbol{e}_Z$.
- Thermal properties are assigned to finite elements/nodes belonging to the support walls and to the powder zone. Note that scalar isotropic conductivities are

used both in walls and powder. The thermal resolution is then performed by a traditional nonlinear thermal solver, until a steady state regime is obtained.

- The homogenized heat flux vector through the RVE is defined as the volume averaged heat flux: $\left(\langle \boldsymbol{q} \rangle = \int_\Omega -\{\kappa\} \nabla T dV\right) / V_\Omega$. $\{\kappa\}$ denotes the local thermal conductivity defined in the level set approach regarding the Heaviside function associated to the wall/powder interface (Chen et al., 2018).

- A diagonal thermal conductivity matrix is assumed as justified in the Appendix A. Consequently, $\langle q \rangle_Z \approx - \langle \kappa \rangle_{ZZ} \nabla T_Z^{imp}$. This leads to the expression of the homogenized vertical conductivity:

$$\langle \kappa \rangle_{ZZ} = \frac{1}{\nabla T_Z^{imp} V_\Omega} \int_\Omega \{\kappa\} \nabla T_Z \, dV \tag{8}$$

- The determined homogenized vertical conductivity $\langle \kappa \rangle_{ZZ}$ is identified for the averaged temperature in Ω domain: $\langle T \rangle = (\int_\Omega T dV)/V_\Omega$. Choosing a small thermal gradient ensures that $\langle \kappa \rangle_{ZZ}$ is determined at the average temperature associated to the two opposite vertical surface, T_{top} and T_{bot}. Here, a temperature difference $T_{top} - T_{bot}$ between the faces is set to only 2 °C to obtain a low gradient, hence minimizing the errors induced by the approximations made later on.

By plotting the numerical values of the homogenized vertical conductivity as a function of temperature, an excellent agreement is observed with the analytical solution (Fig. 4a).

3.2.2. Numerically homogenized horizontal conductivity

The numerical approach used to determine the homogenized horizontal conductivity is similar in every aspect to the one developed for vertical conductivity in section 3.2.1, except that the Dirichlet boundary conditions are no longer applied to the top and bottom faces of the part, but to the two opposite sides in the horizontal direction. The values obtained at different temperatures by this approach are plotted in Fig. 4b (red crosses), where they are compared with the values obtained by the analytical homogenization strategies related to PIS and PFS formulations. As expected, this numerical solution is found between these two extreme solutions. Moreover, it can be seen that the numerical estimate agrees rather well with the harmonic mean based on PIS and PFS solutions, as provided in Eq. 6. This is illustrated in Fig. 4b. This result on one hand validates the developed analytical homogenization solutions, and on the other hand illustrates the potential of the more general numerical homogenization.

3.3. Characterized homogenized tensor and numerical verification

As the support geometry is invariant along Z axis, as given in Fig. 2, a rotation of a single angle θ is enough to define the transformation of the anisotropic thermal conductivity tensor between the RVE reference frame (X, Y, Z) limited by the red contour and the global Cartesian frame (x, y, z). In agreement with ~~Annasabi and Erchiqui~~ Annasabi & Erchiqui (2020), this leads to Eq. 9.

$$\langle \mathbf{K} \rangle_{|xyz} = \mathbf{M}_\theta \, \langle \mathbf{K} \rangle_{|XYZ} \, \mathbf{M}_\theta^T \tag{9}$$

where the transformation matrix from the reference frame to the global Cartesian frame is:

$$\mathbf{M}_\theta = \begin{bmatrix} \cos(\theta) & -\sin(\theta) & 0 \\ \sin(\theta) & \cos(\theta) & 0 \\ 0 & 0 & 1 \end{bmatrix} \tag{10}$$

As discussed in previous subsections, and regarding the equivalence of X and Y axes for heat flow, the homogenized conductivity matrix is diagonal with the same coefficients in XX and YY components. Thereafter, this matrix has the following form:

$$\langle \mathbf{K} \rangle_{|XYZ} = \begin{bmatrix} \langle \kappa \rangle_{XX} & 0 & 0 \\ 0 & \langle \kappa \rangle_{XX} & 0 \\ 0 & 0 & \langle \kappa \rangle_{ZZ} \end{bmatrix} \tag{11}$$

Using Eq. 9, the expression of $\langle \mathbf{K} \rangle_{|xyz}$ can be easily determined for any rotation angle θ. However, as the matrix is diagonal and transverse isotropic in XY plane, same matrix is obtained, independently of the rotation angle θ. Consequently, $\langle \mathbf{K} \rangle_{|xyz} = \langle \mathbf{K} \rangle_{|XYZ}$ for any angle θ.

Following this result, it is interesting to check that it can be effectively retrieved by numerical homogenization. For this, a set of computations are conducted on the RVE defined by the black contour in the right part of Fig. 2b.

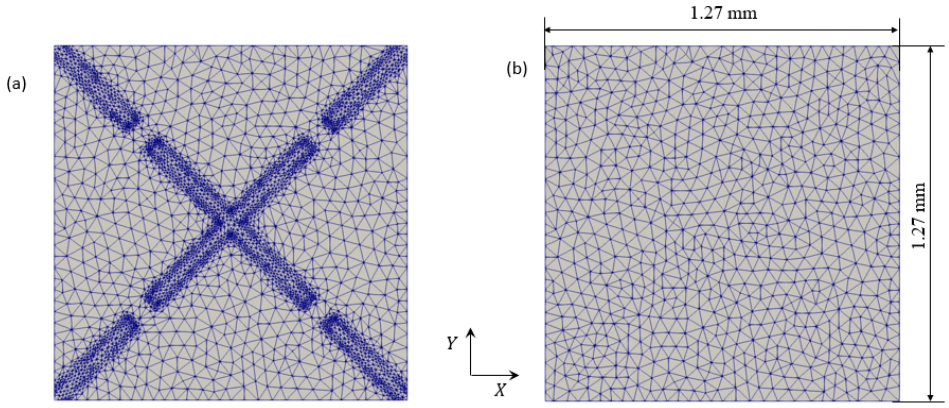

Figure 6. RVE model: (a) mesh of explicit support wall, (b) homogenized mesh

- A first set of two calculations is run on this RVE, similarly to Sections 3.2.1 and 3.2.2, using a vertical (resp. horizontal) temperature gradient along the Z (resp. X) direction. The RVE is meshed finely in order to describe the support walls as presented in the top view of the mesh (Fig. 6 a). These calculations use isotropic scalar conductivities in support walls and powder as in Sections 3.2.1 and 3.2.2.

- A second set of two calculations is run on the same domain, with the same strategy, but ignoring the internal support structure and therefore using a uniform mesh size as presented in Fig. 6 b. The number of elements is reduced from 1.36 million to 0.26 million (Table II). For these two calculations, uniform homogenized values of density, specific heat, and conductivity are chosen.

– For the density, the mass of the domain is expressed by $m = (\rho_w S_w + \rho_p S_p)H$, where $\rho_p = \rho_w(1-\phi)$ with ϕ the porosity (volume fraction of gas in the powder bed). This leads to $\langle\rho\rangle = \rho_w(S_w + (1-\phi)S_p)/S_{tot}$.

– For the specific heat, the approach consists in ensuring that the enthalpy is the same as in the RVE. Considering the respective density and specific heat of support walls and powder, the total enthalpy of the RVE can be expressed, for a temperature T, as $h = \rho_w C_{p,w} T S_w H + \rho_p C_{p,p} T S_p H$, in which we have $C_{p,p} \equiv C_{p,w}$ and still $\rho_p = \rho_w(1-\phi)$. This leads to the following expression for the homogenized specific heat: $\langle C_p\rangle = C_{p,w}(S_w + (1-\phi)S_p)/S_{tot}$.

– Finally, for the conductivity, the coefficients of the homogenized conductivity tensor $\langle\mathbf{K}\rangle_{|xyz} = \langle\mathbf{K}\rangle_{|XYZ}$ are taken from the previous characterization: Section 3.2.

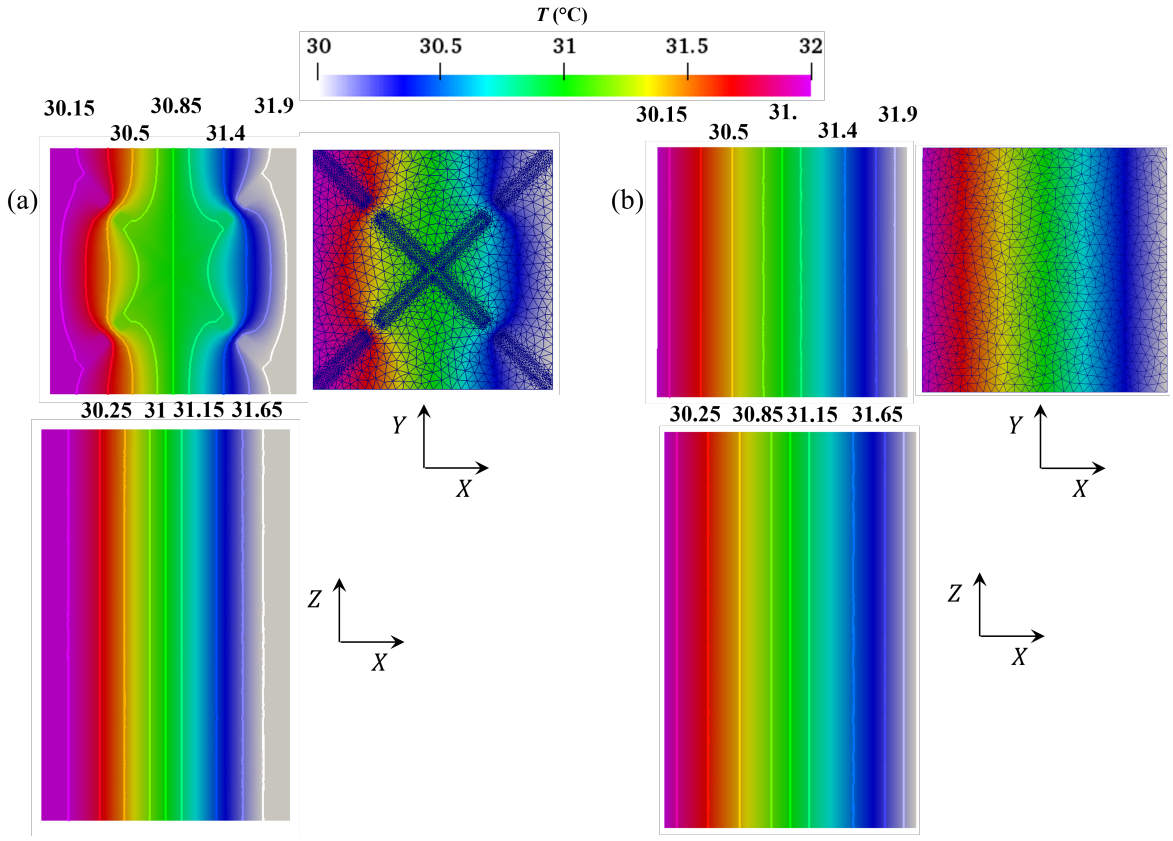

Figure 7. Temperature distribution at steady state (200 s): (a) the RVE with explicit discretization of support walls, and (b) the homogenized material domain. Three different views are given: transverse cross section, without and with mesh (top line), and longitudinal side view (bottom line)

With the above setting, a computational speedup of 6.8 is obtained by the parallel calculation with 28 cores, which is almost linear with a reduced element ratio of 5.2, as shown in Table II. The thermal flux obtained by the two sets of calculations are available in Table II. As expected, the smallest difference is found in the vertical direction, for which the agreement is excellent (relative error 0.07%). In the horizontal direction the difference is higher (relative error 1.05%) but still reasonably low. Note that the uniform Dirichlet boundary conditions that are inherent to this approach are quite severe and

can explain partially this difference. Another contribution could be the influence of the mesh size in the interfacial zone, which has not been studied in the framework of this work. In Fig. 7, comparisons are performed on the steady-state temperature fields

TABLE II. Heat flux (absolute value) through the RVE defined by the black contour

	Explicit support	Homogenization
Number of element, $[\times 10^6]$	1.36	0.26
Computation time, [s]	504	74
$\langle q \rangle_X$, $[\mathrm{W} \cdot \mathrm{m}^{-2}]$	645.4	638.6
$\langle q \rangle_Z$, $[\mathrm{W} \cdot \mathrm{m}^{-2}]$	1224.4	1223.5

obtained under a horizontal temperature gradient. Despite the very similar average heat fluxes $\langle q \rangle_X$ (Table II), the temperature fields are quite different. In the RVE with explicit description of walls (Fig. 7a), the differences in thermal diffusivity between the two domains, walls and powder, clearly appear, leading to strong disorientations of the local temperature gradient near the more conductive walls, also influenced by the small wall interruptions occupied by the far less conductive powder.

In total, these results validate the homogenized model of the thermal conductivity and its numerical implementation in the thermal solver. Consequently, it can be concluded that such supports can indeed be replaced by an equivalent homogenized material in numerical simulation of the L-PBF process.

4. Application to the L-PBF process simulation

4.1. Presentation of the thermal code used for simulation

The simulation is performed with the thermal finite element code previously developed by ~~Zhang et al.~~ Zhang et al. (2018b,a, 2022). As illustrated in Fig. 8, this code allows considering heat exchange in the non-scanned powder, around the part during its construction, thus accounting for a realistic thermal environment of the part, instead of over-simplified boundary conditions that would be applied to its surface. The successive deposition of layers is modelled by updating a level-set function ψ (used to track the interface between the material domain, including the powder bed, and the gas domain, located at the top of the mesh in Fig. 8), and by a volume heat source applied in every newly deposited layer (Zhang et al., 2022). This thermal model presents a high-performance and reliable prediction for both thermal distribution and thermal evolution. In the present study, it is used in its latest version allowing material addition by groups of layers (metalayers, or superlayers) to save computation time while preserving accuracy (Zhang et al., 2022). When using this option, n layers are deposited together at a given time, while the heat input consists of n successive applications of a volume heat source in the metalayer. In the present study, the thermal solver proposed in Zhang et al. (2022) has been adapted to handle a tensorial heat conductivity in place of a scalar one.

4.2. Presentation of the case studied

The studied part is a thin wall of dimension $30 \times 2 \times 25$ mm^3 ($L \times W \times H$), see Fig. 8 (constructed part). Two cases are considered: without support and with a

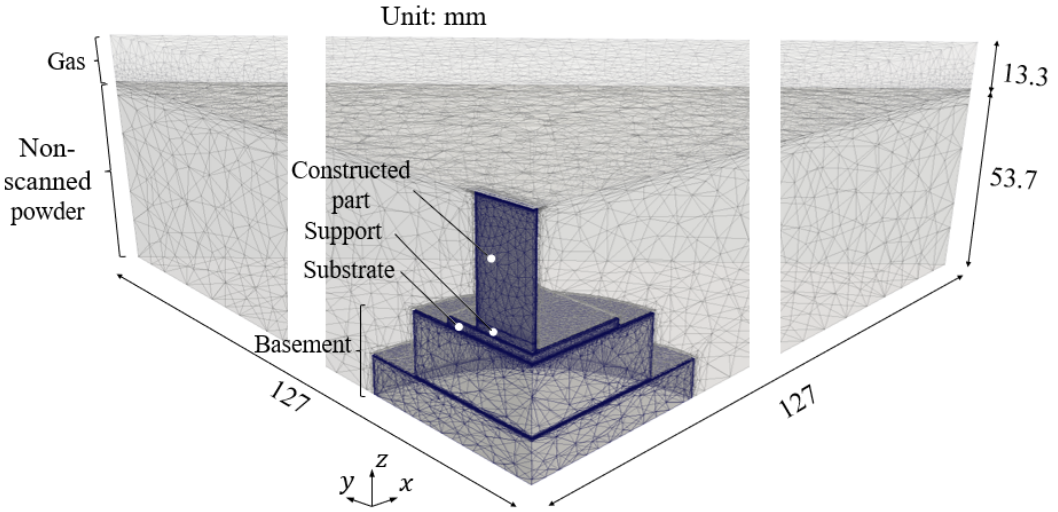

Figure 8. Geometry of FE modeling: one quarter of the total part

support of 2 mm height between substrate and part by cross lattice (as given in Fig. 2a). In the simulation, the support is assumed as a homogenized anisotropic material. Its homogenized properties $\langle\rho\rangle$, $\langle C_p\rangle$, $\langle\mathbf{K}\rangle$ are explained in Section 3.3. The metallic material is the nickel-based alloy IN738LC and the gas is argon. All material data are given in the left part of Table III.

As illustrated in Fig. 8, the simulation encompasses the part to be built, the support structure, a substrate plate and two basement blocks. To reduce the computational cost, only a quarter of the original geometry is simulated due to the symmetry of the selected structure. According to Table II, approximately 50 million elements would be required for the explicit support structure in the entire support zone $30 \times 2 \times 2$ mm^3. Using the homogenized approach, only 70000 elements are required in the support zone, where only a fine mesh is needed for the interface between the support and the surrounding zones.

In terms of resolution of heat conservation equations, the equivalent thermal conductivity matrix in the global Cartesian frame is implemented in the non-linear thermal solver (Eq. 12):

$$\frac{\partial\{\rho h\}}{\partial t} - \nabla\cdot\left(\left\{\mathbf{K}_{|xyz}\right\}\cdot\nabla T\right) = \dot{Q}_V \tag{12}$$

where ρ is the density, h is the mass enthalpy, $\mathbf{K}_{|xyz}$ is the thermal conductivity matrix in the global Cartesian frame, T is the temperature field, $\dot{Q}_V$ is the volume heat source. The braces $\{\}$ correspond to the properties averaging associated to the gas and the matter, this latter being defined by the powder, support and part. Regarding the matrix $\mathbf{K}_{|xyz}$, for the support structure, the anisotropic homogenized matrix presented in Eq. 9 is used. The other parts are assumed as isotropic materials. Consequently, their matrix conductivity is defined as $\left\{\mathbf{K}_{|xyz}\right\} = \{\kappa\}\,\mathbf{I}$. The scalar $\{\kappa\}$ is the local mixed thermal conductivity and $\mathbf{I}$ is the unit tensor.

4.3. Energy input

As already presented in Zhang et al. (2022), for each layer in a metalayer, the energy which is delivered by the laser during the time required to scan the layer, t_{scan},

is replaced by an equivalent volume heat source $\dot{Q}_V$ uniformly applied within the layer volume (V_{layer}) during a short time t_{heat}, with $t_{heat} \ll t_{scan}$. Therefore, $\dot{Q}_V$ is formulated by:

$$P_L(1-R)t_{scan} = \dot{Q}_V V_{layer} t_{heat} \tag{13}$$

where P_L is the power of the laser, R is the material's reflection coefficient. Note that the scanned area being equal to $H_D v_L t_{scan}$ with H_D the hatch distance, then the layer volume can be calculated by $V_{layer} = (H_D v_L t_{scan})\,\Delta z$. As a result, the volume heating source is also expressed by:

$$\dot{Q}_V = \frac{P_L\ (1-R)}{t_{heat}\ v_L\ H_D\ \Delta z} \tag{14}$$

The heating time is defined as a multiple of the real exposure time of the powder bed: $t_{heat} = n_L \phi_L / v_L$, with ϕ_L the laser spot diameter and v_L the laser velocity. In the present study, n_L is taken equal to 400, corresponding to $t_{heat} = 0.09$ s. A discussion on the influence of n_L can be found in Zhang et al. (2018b). Following this short heat input, a cooling time t_{cool} is considered as the complementary part compared to the heating time t_{heat}, so that we have $t_{scan} = t_{heat} + t_{cool}$. In addition, between two layers, the whole system cools during the dwell-time (the time required to spread a new layer of powder): t_D. Because the simulation domain is large enough and the consideration of non-scanned powder, adiabatic boundary conditions are applied to the lateral surfaces. However, the convective heat exchange is considered at the bottom surface of the substrate by

$$-\kappa \nabla T \cdot \boldsymbol{n} = h_{conv.}(T - T_{ext}) \tag{15}$$

where $h_{conv.}$ is the heat exchange coefficient, T_{ext} is the air temperature, and $\boldsymbol{n}$ is the unit outward normal vector. In addition, the adiabatic boundary condition is applied to the top surface of the entire domain. The nickel based super alloy IN738LC is adopted for the powder bed, substrate and basement. Material and Gas properties are given in the left part of Table III. The properties related to thermal conductivity, the phase transformation and enthalpy evolution are adopted from the work of ~~Grange et al.~~ Grange et al. (2021), while the thermal conductivity of powder bed is calculated by the model from ~~Hadley~~ Hadley (1986) with a porosity of 0.5. The convective coefficient $h_{conv.}$ was calibrated during the internship work of ~~Navarre-Lasnier~~ Navarre-Lasnier (2022). The parameters related to the process are given in the right part of Table III. For the deposition of layer thickness $\Delta z = 25$ µm, a total of 1000 layers is considered. The process simulation is performed with the C++ library CimLib developed at CEMEF. For one process simulation, the calculation time is around 26 h with 28 cores under parallel calculation with an Intel Xeon E5-2680v4 processor.

4.4. Simulation results and discussion

To study the effect of the support structure, the temperature profile along line variation, temperature evolution at chosen points and energy loss through the bottom

TABLE III. Properties and Parameters used for material and process simulation

Thermal properties			Process parameters	
Material	Variable	Value	Variable	Value
IN738LC	*Temperature*, [°C]		Laser diameter, ϕ_L, [µm]	180
	Solidus, T_s	1216	Layer thickness, Δz, [µm]	25
	Liquidus, T_l	1341	Hatch distance, H_D, [µm]	105
	Density, [$\mathrm{kg\,m^{-3}}$]			
	Solid phase, ρ_s	7659	Laser power, P_L, [W]	250
	Liquid, ρ_l	7118	Scanning speed, v_L, [$\mathrm{mm\,s^{-1}}$]	800
	Heat capacity, [$\mathrm{J\,kg^{-1}\,K^{-1}}$]			
	Solid, $C_{p,s}$	643	Dwell time, t_D, [s]	8.5
	Liquid, $C_{p,l}$	754	Reflection coeff., R	0.55
	Thermal conductivity, [$\mathrm{W\,K^{-1}\,m^{-1}}$]			
	Dense material, κ_s	Grange et al. (2021)		
	Powder, κ_p	Hadley (1986)		
	Convective coeff., $h_{conv.}$, [$\mathrm{W\,K^{-1}\,m^{-2}}$]	100		
Gas	Density, ρ_g, [$\mathrm{kg\,m^{-3}}$]	1.3		
	Heat capacity, $C_{p,g}$, [$\mathrm{J\,kg^{-1}\,K^{-1}}$]	1000		
	Thermal conductivity, κ_g, [$\mathrm{W\,K^{-1}\,m^{-1}}$]	0.024		

surface are extracted.

4.4.1. Vertical profiles

Firstly, a vertical temperature profile observed at different stages of the part construction is presented for the two options considered (with and without support). The vertical profile is positioned at the center of the part, that is at the intersection between the two symmetry planes limiting the one-quarter configuration studied (see Fig. 8). On this profile, the zero reference point is located at 2 mm below the substrate, in the basement. The vertical profile goes through the basement, the substrate, the support zone when it is present, and the constructed part. Comparisons are made for the same process parameters with and without support. It should be noted that the part with support is always 2 mm higher (which corresponds to the support height of 2 mm under the part).

Figure 9 presents vertical temperature profiles at the beginning of the construction: part height 1 mm. In the left part of the figure (Fig. 9a) the profiles are plotted at the end of the deposition of layer 40, i.e. metalayer 4 (with 10 layers per metalayer), whereas in the right part of the figure (Fig. 9b) they are plotted at the end of the dwell time following this deposition.

The blue curves go up to a higher z coordinate, as the part is built on the support of 2 mm. Several observations can be made from these curves:

- Firstly, the support acts as a 'thermal barrier'. Comparing the two profiles in Fig. 9a, it appears that heat is retained within the part when the support is present.

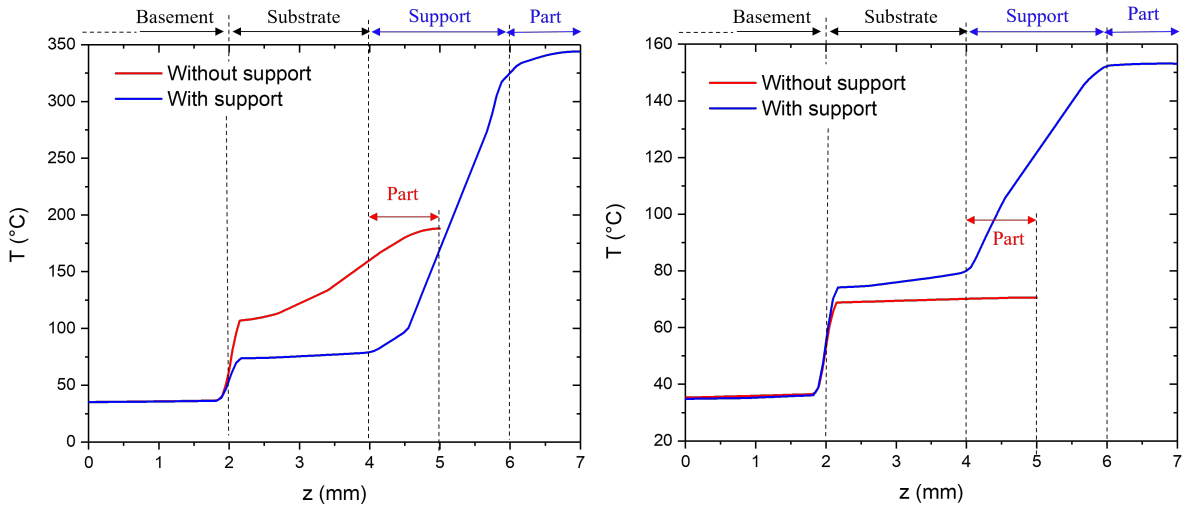

(a) After scanning of current layer

(b) After dwell time

Figure 9. Vertical temperature profiles at the beginning of the construction: build height 1mm

As a consequence, the temperatures are significantly higher in the part when the support is present. Accordingly, the temperatures in the substrate are lower.

- The presence of support also decreases the temperature gradients, both in the substrate and in the part. In the part the temperature difference between top and bottom is decreased from about 30 °C (without support) to about 20 °C (with support). This effect is more marked in the substrate, where the temperature difference is decreased from about 50 °C (without support) to only a few degrees (with support).

- It is worth noting the high temperature gradient within the support itself, with a vertical temperature difference of about 280 °C within a 2 mm height.

- After the dwell time (see profiles in Fig. 9b), it can be observed that without support, the temperature gradients have disappeared in both the part and the substrate, while a temperature difference remains between the substrate and the basement, because of the thermal resistance at their interfaces with a value of $5 \cdot 10^3$ W K^{-1} (Aalilija et al., 2021; Navarre-Lasnier, 2022). Conversely, in presence of support, the part is still found hotter than the substrate, even if it is now almost free of temperature gradient. Note that the temperature difference within the support has decreased from about 240 °C at the end of deposition to about 70 °C after dwell time.

Figure 10 shows vertical temperature profiles inside the constructed part ($z = 0$ now corresponding to the bottom of the constructed part) at 2 different construction stages: intermediate (part height 15mm) in Fig. 10a and final (part height 25 mm) in Fig. 10b. All profiles are plotted after the dwell time. It can be seen that the addition of support has little impact on the shape of the temperature profile in the part, but that it does create an offset (linked to the thermal barrier effect), which is more pronounced at the bottom of the part ($z = 0$). This offset becomes less pronounced as construction progresses: 82 °C offset at 1 mm (see Fig. 9b), 57 °C offset at 15 mm (Fig. 10a), and

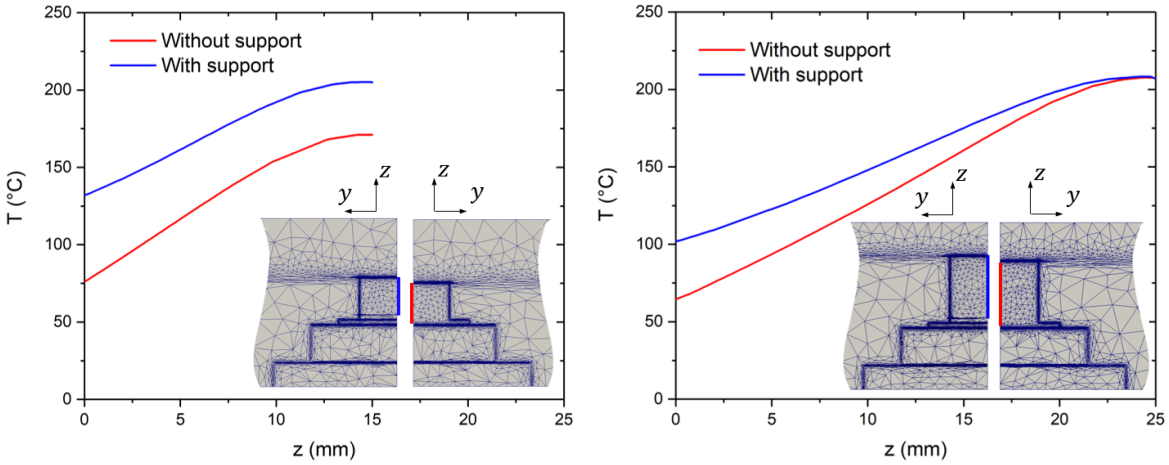

(a) Construction height 15mm

(b) Construction height 25mm

Figure 10. Vertical temperature profiles after dwell time at two different construction stages: intermediate and final

finally 37 °C at the end of construction (height 25 mm, Fig. 10b). It is also worth noting that the impact of the support is still very visible even after 25mm construction, which corresponds to the deposition of 1000 layers. Moreover, with support, the temperature at the construction front is nearly constant: 205 °C at 15 mm, 207 °C at 25 mm. It helps the construction front reach the steady state much faster than the one without the support structure.

4.4.2. Horizontal profiles

Horizontal temperature profiles are defined at the construction front, starting from the center of the part and extending along direction x, (as defined in Fig. 11a). Profiles extend through half the thickness of the part (1 mm) and through the powder zone (14 mm) over a total horizontal length of 15 mm. In Fig. 11, the horizontal profiles are plotted after the latest layer deposition (before dwell time) for different construction heights of the constructed part: 1 mm, 15 mm and 25 mm (corresponding to the previous subsection), with and without the support structure.

Looking at these plots, it can be seen that as expected, the heat extraction in the part constructed without support is much faster than with support. However, what is noticeable is that this extraction proceeds mainly through the center of the part than through the regions in contact with the non-scanned powder. This results from the concurrent effect of a low diffusivity in the powder domain, due to a lower heat conductivity, and of a higher diffusivity in the dense metal. The effect is particularly visible at the early stages of construction (Fig. 11b, height 1 mm) without support.

Figure 12 shows the same charts as Fig. 11, but after dwell time. The thermal peaks at the part/powder interface are not visible any more for the three different deposition heights. Like in Fig. 10, it can be seen that the impact of the support decreases with the progress of the construction. It is almost not perceptible at the end of the construction. The temperature difference at the center of the part ($x = 0$) is changed from near 82 °C at the beginning to less than 1 °C at the end.

This effect is less marked when the support is present: in this case, the thermal diffusion is considerably attenuated by the support and there is less gradient inversion in

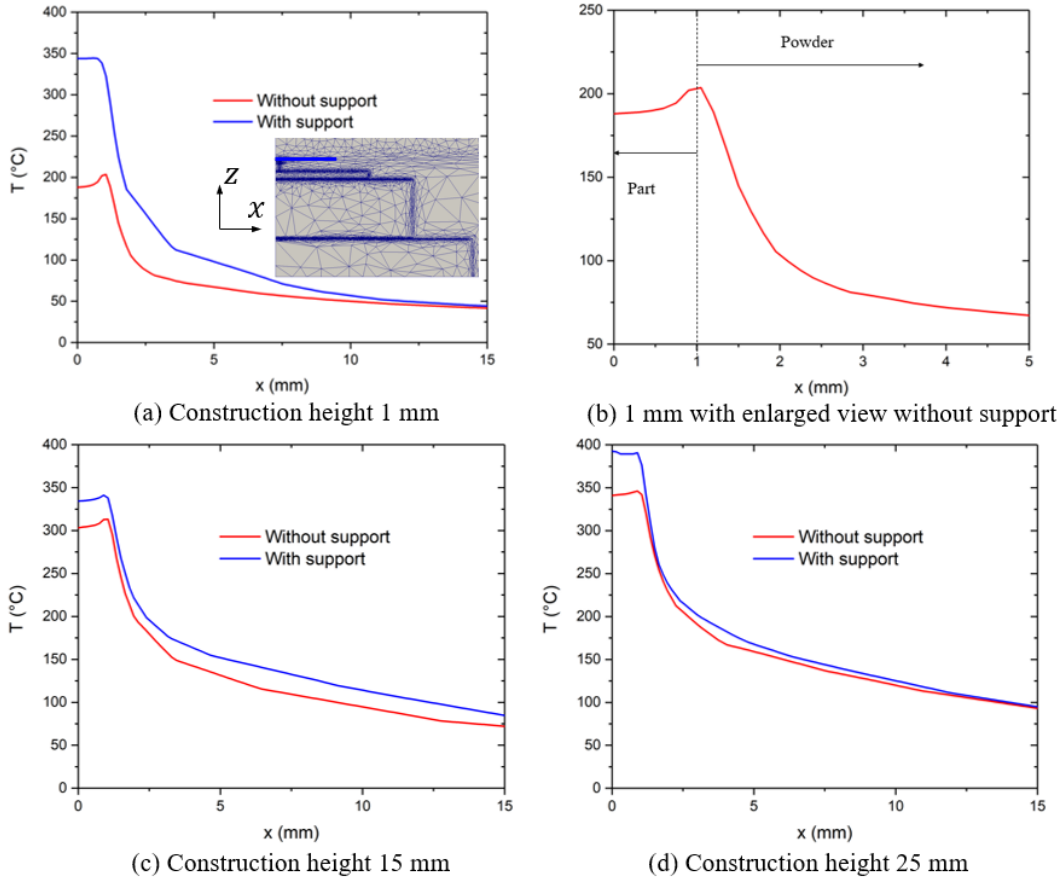

Figure 11. Horizontal temperature profiles after layer scanning (before dwell time) after different construction height

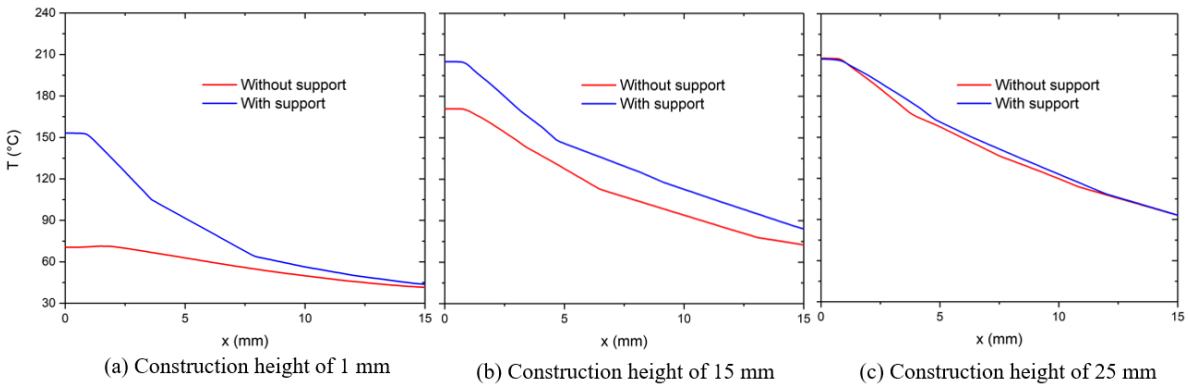

Figure 12. Horizontal profiles after dwell time for different deposition heights

the powder. This effect diminishes as manufacturing progresses, and tends to disappear at 25 mm construction height.

4.4.3. Energy and temperature evolution

The results in Fig. 11 have highlighted that the support acts like a thermal resistance preventing the part from transferring its thermal energy to the substrate. Therefore, it can be inferred that the part with support evacuates more heat to the powder than the part without support. To verify this point, the total amount of energy evacuated

by convection through the bottom surface of the basement is plotted in Fig. 13a. In addition, the temperature evolution throughout the manufacturing process at an anchored point located at the bottom center of the substrate, is plotted in Fig. 13b.

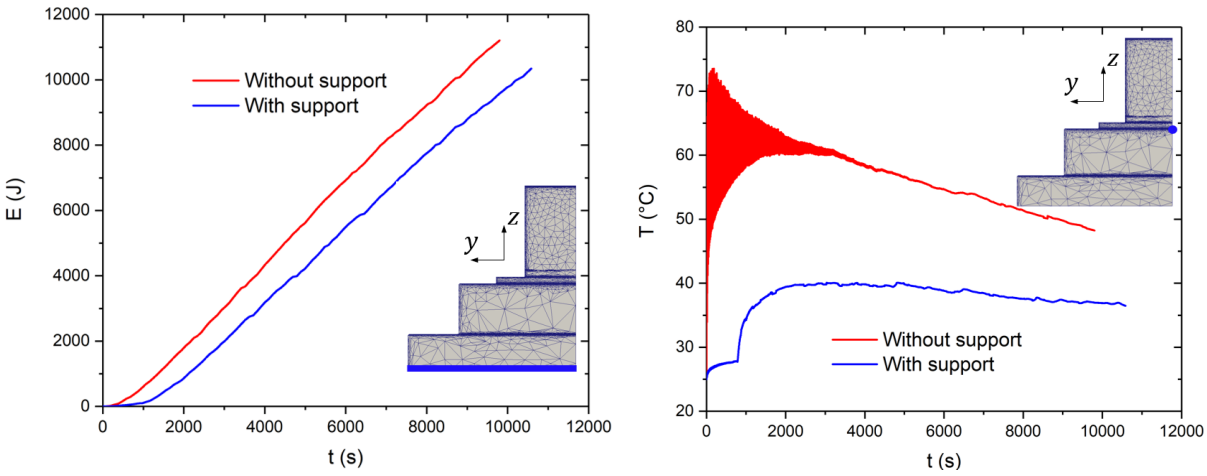

(a) Energy loss (b) Temperature evolution

Figure 13. Evolutions of energy loss and temperature at the bottoms of basement and substrate, respectively

Fig. 13a highlights the expected effect: the amount of energy evacuated from the bottom of the basement is higher in the case of the construction without support. This results from two combined effects: on one hand, the extracted power is continuously lower in the support case (but the difference appears to be small: see the comparable slopes of the two curves), and on the other hand, a significant part of difference in heat extraction is due to the effect of the support at the beginning of the construction, when it creates an offset time during which heat extraction is considerably reduced. In Fig. 13b, the offset effect is even more clearly evidenced: a significant jump in temperature evolution is observed at the start of part construction, explained by the fact that more energy is deposited for part construction than for support construction (section 4.3) at the initial stage. Therefore, the cycling temperature is considerably higher in the non-supported case during this initial stage. Later in the construction, it can be seen that the cycling effect progressively vanishes, as the construction front moves away from the measuring point. However, the temperature still remains higher in the unsupported case.

5. Conclusion and perspectives

This paper has reported first on methods that can be used to characterize the homogenized, and generally anisotropic, heat conductivity of support structures used in L-PBF additive manufacturing. Selecting a support structure with a simple representative volume element (RVE), it was shown how traditional analytical modeling of heat transfer can be used to determine the different components of an anisotropic heat conductivity tensor. This was validated by performing this characterization by finite element modeling applied to the same RVE. The principles of FEM identification being quite general, it was also shown how numerical characterization can be envisaged for any support structure based on a periodic three-dimensional pattern, first in a reference

frame associated with this pattern, and in a second step in the reference frame related to the L-PBF additive manufacturing process to be numerically simulated.

Still considering the same simple support structure, a simple L-PBF construction was studied by FEM simulation, the objective being to illustrate the impact of the use of a support structure on heat transfer through the different domains (part, non-scanned powder, substrate), and so on the thermal history of the part during its construction. The anisotropic thermal barrier effect of the support structure, due to the very high volume fraction of non-scanned powder in it, was effectively observed.

Compared to the same construction without support structure, the simulation evidenced the effects induced by the thermal barrier: higher temperatures in the part, lower temperature gradients in the part, less noticeable local effects at the interface between the part and the surrounding non-scanned powder. The simulation also showed that these effects are progressively attenuated as construction progresses. It is important to remember that the intended properties of a lattice structure can be impacted by the details of its printing process. This is especially true for the type of support structure studied here, based on thin solid walls.

In total, this study helps understanding how numerical identification and anisotropic heat transfer FEM modelling could help process engineers to better design and use support structures in view of better controlling heat transfer in L-PBF manufacturing. An optimized thermal control is key to reduce cracking occurrence, and to control metallurgical evolutions during manufacturing, and thus final properties.

Acknowledgment

The authors would like to thank their colleagues at MINES Paris, PSL University, Centre des Materiaux, CNRS UMR 7633, for discussing the proposed cross-support: Jean-Dominique BARTOUT and Christophe COLIN. We are also grateful for the financial support of SAFRAN and ANR-JCJC Gramme.

Appendix A. Numerical justification of the assumption of neglecting the non-diagonal coefficients of $\kappa|_{XYZ}$

Now that the coefficients $\langle\kappa\rangle_{XX} = \langle\kappa\rangle_{YY}$ and $\langle\kappa\rangle_{ZZ}$ have been determined, we can turn our attention to other coefficients of the matrix. Here is a reminder of $\kappa|_{XYZ}$:

$$\kappa|_{XYZ} = \begin{bmatrix} \langle\kappa\rangle_{XX} & \langle\kappa\rangle_{XY} & \langle\kappa\rangle_{XZ} \\ \langle\kappa\rangle_{YX} & \langle\kappa\rangle_{YY} & \langle\kappa\rangle_{YZ} \\ \langle\kappa\rangle_{ZX} & \langle\kappa\rangle_{ZY} & \langle\kappa\rangle_{ZZ} \end{bmatrix}_{(XYZ)} \tag{A.1}$$

Next, it will be shown that the off-diagonal coefficients are ignored. This can confirm the hypotheses used in Eq. 11. The numerical model presented in section 3.2.2 is adopted, in which a temperature gradient is imposed on two opposite faces using Dirichlet conditions. Fourier's law is recalled in its matrix form from Eq. 7 . The heat flux vector can be determined numerically using the Eq. 8. When a gradient $\partial T/\partial X$ is imposed, the flux in other directions is nearly zero. For $T = 30\,°\mathrm{C}$, the following values are obtained when imposing a X gradient:

$$\begin{bmatrix} \langle q\rangle_X \\ \langle q\rangle_Y \\ \langle q\rangle_Z \end{bmatrix} = \begin{bmatrix} 903 \\ 0.068 \\ -0.03 \end{bmatrix} (W/m^2) \tag{A.2}$$

The temperature profile at the steady state associated with this calculation can be seen in Fig. A.1. The parallel isothermal surfaces are observed near two surfaces normal to Y axis, while the parallel heat flux surfaces are found near cross edges.

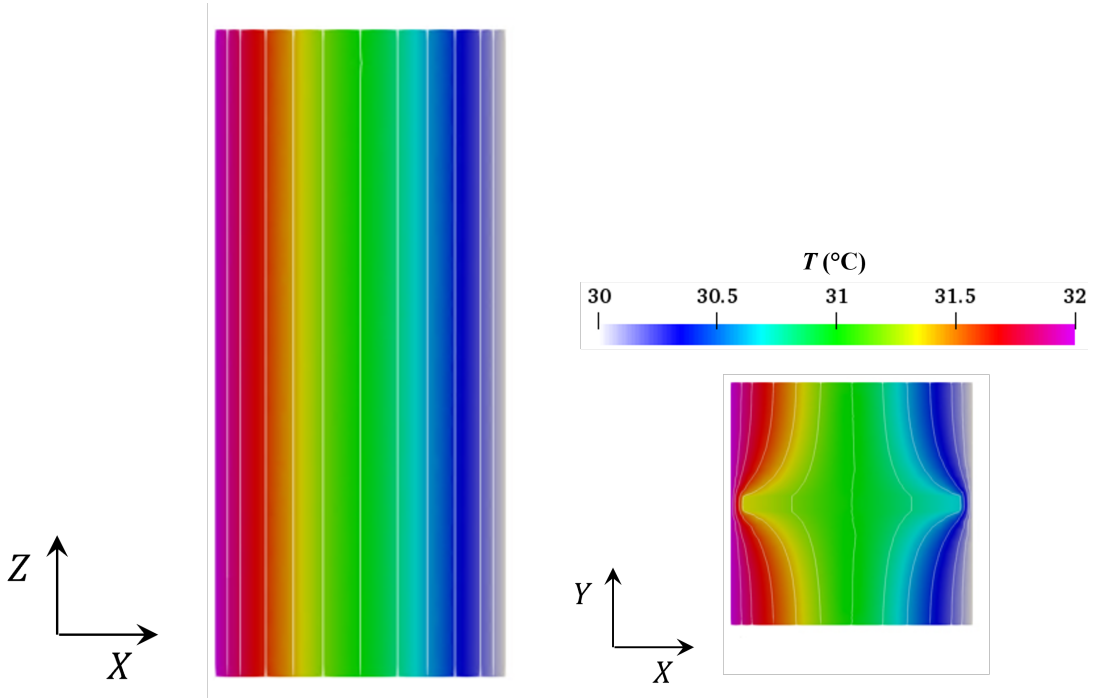

(a) Front view (b) Top view

Figure A.1. Numerical temperature field at the steady state

Thus, by developing the equations contained in the matrix system in Eq. 7, below

equation is obtained:

$$\begin{cases} -\langle\kappa\rangle_{XX}\frac{\partial T}{\partial X} \approx \langle q\rangle_X \\ -\langle\kappa\rangle_{XY}\frac{\partial T}{\partial X} \approx 0 \\ -\langle\kappa\rangle_{XZ}\frac{\partial T}{\partial X} \approx 0 \end{cases} \tag{A.3}$$

Hence:

$$\begin{cases} \langle\kappa\rangle_{XY} \approx 0 \\ \langle\kappa\rangle_{XZ} \approx 0 \end{cases} \tag{A.4}$$

Similarly, by repeating the operation and imposing a gradient $(\partial T/\partial Y)_{imp}$, $\langle\kappa\rangle_{YZ} \approx 0$ is obtained.

Due to the symmetry of the thermal conductivity matrix, all off-diagonal coefficients are relatively close to zero. This proves that the assumption of neglecting the off-diagonal coefficients is reasonable.

References

Aalilija, A., Gandin, C.-A., & Hachem, E. (2021). A simple and efficient numerical model for thermal contact resistance based on diffuse interface immersed boundary method. *International Journal of Thermal Sciences*, *166*, 106817. doi:10.1016/j.ijthermalsci.2020.106817.

Al Amin, A., Sabri, L., Poole, C., Baig, T., Deissler, R., Rindfleisch, M., Doll, D., Tomsic, M., Akkus, O., & Martens, M. (2018). Computational homogenization of the elastic and thermal properties of superconducting composite MgB2 wire. *Composite Structures*, *188*, 313–329. doi:10.1016/j.compstruct.2017.12.060.

Annasabi, Z., & Erchiqui, F. (2020). 3D hybrid finite elements for anisotropic heat conduction in a multi-material with multiple orientations of the thermal conductivity tensors. *International Journal of Heat and Mass Transfer*, *158*, 119795. doi:10.1016/j.ijheatmasstransfer.2020.119795.

Burger, N., Laachachi, A., Ferriol, M., Lutz, M., Toniazzo, V., & Ruch, D. (2016). Review of thermal conductivity in composites: Mechanisms, parameters and theory. *Progress in Polymer Science*, *61*, 1–28. doi:10.1016/j.progpolymsci.2016.05.001.

Chen, Q., Guillemot, G., Gandin, C.-A., & Bellet, M. (2018). Numerical modelling of the impact of energy distribution and Marangoni surface tension on track shape in selective laser melting of ceramic material. *Additive Manufacturing*, *21*, 713–723. doi:10.1016/j.addma.2018.03.003.

Chen, S. (2019). *Investigation of FEM Numerical Simulation for the Process of Metal Additive Manufacturing in Macro Scale*. Ph.D. thesis INSA Lyon.

El Moumen, A., Kanit, T., Imad, A., & El Minor, H. (2015). Computational thermal conductivity in porous materials using homogenization techniques: Numerical and statistical approaches. *Computational Materials Science*, *97*, 148–158. doi:10.1016/j.commatsci.2014.09.043.

Gori, F., & Corasaniti, S. (2014). Effective thermal conductivity of composites. *International Journal of Heat and Mass Transfer*, *77*, 653–661. doi:10.1016/j.ijheatmasstransfer.2014.05.047.

Grange, D., Queva, A., Guillemot, G., Bellet, M., Bartout, J.-D., & Colin, C. (2021). Effect of processing parameters during the laser beam melting of Inconel 738: Comparison between simulated and experimental melt pool shape. *Journal of Materials Processing Technology*, *289*, 116897. doi:10.1016/j.jmatprotec.2020.116897.

Hadley, G. R. (1986). Thermal conductivity of packed metal powders. *Int. J. Heat Mass Transfer*, *29*, 909–920. doi:10.1016/0017-9310(86)90186-9.

He, Y., & Webler, B. (2022). A solidification mode selection process map for laser powder bed fusion additive manufacturing of B-modified Ti6Al4V. *Additive Manufacturing*, *59*, 103086. doi:10.1016/j.addma.2022.103086.

Jarvinen, J.-P., Matilainena, V., Li, X., Piili, H., Salminen, A., Makela, I., & Nyrhila, O. (2014). Characterization of effect of support structures in laser additive manufacturing of stainless steel. *Physics Procedia*, *56*, 72–81. doi:10.1016/j.phpro.2014.08.099.

Jin, L., Zhang, R., & Du, X. (2017). Computational homogenization for thermal conduction in heterogeneous concrete after mechanical stress. *Construction and Building Materials*, *141*, 222–234. doi:10.1016/j.conbuildmat.2017.03.016.

Kajima, Y., Takaichi, A., Nakamoto, T., Kimura, T., Kittikundecha, N., Tsutsumi, Y., Nomura, N., Kawasaki, A., Takahashi, H., Hanawa, T., & Wakabayashi, N. (2018). Effect of adding support structures for overhanging part on fatigue strength in selective laser melting. *Journal of the Mechanical Behavior of Biomedical Materials*, *78*, 1–9. doi:10.1016/j.jmbbm.2017.11.009.

Khobzi, A., Farhang Mehr, F., Cockcroft, S., Maijer, D., Sing, S. L., & Yeong, W. Y. (2022). The role of block-type support structure design on the thermal field and deformation in components fabricated by laser powder bed fusion. *Additive Manufacturing*, *51*, 102644. doi:10.1016/j.addma.2022.102644.

Krakhmalev, P., & Kazantseva, N. (2021). 8 - Microstructure of L-PBF alloys. In I. Yadroitsev, I. Yadroitsava, A. du Plessis, & E. MacDonald (Eds.), *Fundamentals of Laser Powder Bed Fusion of Metals* Additive Manufacturing Materials and Technologies (pp. 215–243). Elsevier. doi:10.1016/B978-0-12-824090-8.00018-4.

Liang, X., Dong, W., Hinnebusch, S., Chen, Q., Tran, H. T., Lemon, J., Cheng, L., Zhou, Z., Hayduke, D., & To, A. C. (2020). Inherent strain homogenization for fast residual deformation simulation of thin-walled lattice support structures built by laser powder bed fusion additive manufacturing. *Additive Manufacturing*, *32*, 101091. doi:10.1016/j.addma.2020.101091.

Liu, X., & Shapiro, V. (2016). Homogenization of material properties in additively manufactured structures. *Computer-Aided Design*, *78*, 71–82. doi:10.1016/j.cad.2016.05.017.

Mahadevan, S., Nath, P., & Hu, Z. (2022). Uncertainty Quantification for Additive Manufacturing Process Improvement: Recent Advances. *ASCE-ASME J Risk and Uncert in Engrg Sys Part B Mech Engrg*, *8*, 010801. doi:10.1115/1.4053184.

March, N. G., Gunasegaram, D. R., & Murphy, A. B. (2023). Evaluation of computational homogenization methods for the prediction of mechanical properties of additively manufactured metal parts. *Additive Manufacturing*, *64*, 103415. doi:10.1016/j.addma.2023.103415.

Martin, J., Yahata, B., Hundley, J., Mayer, J., Schaedler, T., & Pollock, T. (2017). 3D printing of high-strength aluminium alloys. *Nature volume*, *549*, 365–369. doi:10.1038/nature23894.

Nakayama, A. (2023). Chapter two - effective thermal conductivity of porous media. *Advances in Heat Transfer*, *56*, 51–111. doi:10.1016/bs.aiht.2023.05.006.

Navarre-Lasnier, G. (2022). *Simulation of an additive manufacturing process by coupling a finite element model with a cellular automaton model and experimental validation*. Internship report MINES Paris, PSL University.

Subedi, S. C., Shahba, A., Thevamaran, M., Thoma, D. J., & Suresh, K. (2022). Towards the optimal design of support structures for laser powder bed fusion-based metal additive manufacturing via thermal equivalent static loads. *Additive Manufacturing*, *57*, 102956. doi:10.1016/j.addma.2022.102956.

Terada, K., Hori, M., Kyoya, T., & Kikuchi, N. (2000). Simulation of the multi-scale convergence in computational homogenization approaches. *International Journal of Solids and Structures*, *37*, 2285–2311. doi:10.1016/S0020-7683(98)00341-2.

Wang, M., & Pan, N. (2008). Predictions of effective physical properties of complex multiphase materials. *Materials Science and Engineering: R: Reports*, *63*, 1–30. doi:10.1016/j.mser.2008.07.001.

Willot, F., Gillibert, L., & Jeulin, D. (2013). Microstructure-induced hotspots in the thermal and elastic responses of granular media. *International Journal of Solids and Structures*, *50*, 1699–1709. doi:10.1016/j.ijsolstr.2013.01.040.

Wu, T., Temizer, I., & Wriggers, P. (2013). Computational thermal homogenization of concrete. *Cement and Concrete Composites*, *35*, 59–70. doi:10.1016/j.cemconcomp.2012.08.026.

Yang, G., Li, H., Li, Z., Zhu, Z., Liu, R., Zhang, Q., Liu, Y., & Yao, J. (2023). Support design of overhanging structure for laser powder bed fusion. *Journal of Materials Research and Technology*, *24*, 8693–8702. doi:10.1016/j.jmrt.2023.05.087.

Yue, D., Qin, R., Li, D., Wang, Z., Zhang, X., & Chen, B. (2023). Numerical investigation of block support structures with different dimension parameters in laser powder bed fusion of AlSi10Mg. *Results in Physics*, *44*, 106204. doi:10.1016/j.rinp.2022.106204.

Zeng, K., Pal, D., Teng, C., & Stucker, B. E. (2015). Evaluations of effective thermal conductivity of support structures in selective laser melting. *Additive Manufacturing*, *6*, 67–73. doi:10.1016/j.addma.2015.03.004.

Zhang, J., & Li, B. (2022). The influence of laser powder bed fusion (L-PBF) process parameters on 3D-printed quality and stress-strain behavior of high-entropy alloy (HEA) rod-lattices. *Metals*, *12*. doi:10.3390/met12122109.

Zhang, Y., Chen, Q., Guillemot, G., Gandin, C.-A., & Bellet, M. (2018a). Numerical modelling of fluid and solid thermomechanics in additive manufacturing by powder-bed fusion: Continuum and level set formulation applied to track- and part-scale simulations. *Comptes Rendus. Mécanique*, *346*, 1055–1071. doi:10.1016/j.crme.2018.08.008.

Zhang, Y., Gandin, C.-A., & Bellet, M. (2022). Finite element modeling of powder bed fusion at part scale by a super-layer deposition method based on level set and

mesh adaptation. *Journal of Manufacturing Science and Engineering*, *144*, 051001. doi:10.1115/1.4052386.

Zhang, Y., Guillemot, G., Bernacki, M., & Bellet, M. (2018b). Macroscopic thermal finite element modeling of additive metal manufacturing by selective laser melting process. *Computer Methods in Applied Mechanics and Engineering*, *331*, 514–535. doi:10.1016/j.cma.2017.12.003.